applied sciences

MDPI

Article

Investigation of Thermal Effects of Radiofrequency Ablation Mediated with Iron Oxide Nanoparticles Dispersed in Agarose and Chitosan Solvents

Zhannat Ashikbayeva [1,*], Arman Aitkulov [1], Alexey Wolf [2,3], Alexander Dostovalov [2,3], Aida Amantayeva [1], Aliya Kurbanova [4], Vassilis J. Inglezakis [5] and Daniele Tosi [1,4]

[1] School of Engineering and Digital Sciences, Nazarbayev University, 53 Kabanbay Batyr Ave., Nur-Sultan 010000, Kazakhstan; arman.aitkulov@nu.edu.kz (A.A.); aida.amantayeva@nu.edu.kz (A.A.); daniele.tosi@nu.edu.kz (D.T.)
[2] Physics Department, Novosibirsk State University, 1 Pirogov St., 630090 Novosibirsk, Russia; alexey.a.wolf@gmail.com (A.W.); dostovalov@iae.nsk.su (A.D.)
[3] Institute of Automation and Electrometry of the SB RAS, 1 Academician Koptyug Ave., 630090 Novosibirsk, Russia
[4] PI National Laboratory Astana, Nazarbayev University, 53 Kabanbay Batyr Ave., Nur-Sultan 010000, Kazakhstan; aliya.kurbanova@nu.edu.kz
[5] Department of Chemical and Process Engineering, University of Strathclyde, 75 Montrose St., Glasgow G1 1XJ, UK; vasileios.inglezakis@strath.ac.uk
* Correspondence: zhashikbayeva@nu.edu.kz; Tel.: +7-7752926556

check for updates

Citation: Ashikbayeva, Z.; Aitkulov, A.; Wolf, A.; Dostovalov, A.; Amantayeva, A.; Kurbanova, A.; Inglezakis, V.J.; Tosi, D. Investigation of Thermal Effects of Radiofrequency Ablation Mediated with Iron Oxide Nanoparticles Dispersed in Agarose and Chitosan Solvents. *Appl. Sci.* **2021**, *11*, 2437. https://doi.org/10.3390/app11052437

Academic Editor: Greta Varchi

Received: 11 January 2021
Accepted: 16 February 2021
Published: 9 March 2021

Abstract: Thermal ablation (TA) is known as an alternative therapy to surgery to treat tumors. However, TA-based therapy requires advanced approaches in order to prevent causing damage to healthy tissue around the tumor and selectively target the desired area. Nanoparticles are considered as a promising tool in biomedicine to fulfill these requirements. This study was carried out in order to analyze the effect of iron oxide nanoparticles on the temperature increment during radiofrequency ablation therapy of porcine liver. In addition, this research aimed to experimentally evaluate the impact of two solvents such as agarose and chitosan on the temperature change, when magnetic nanoparticles were dispersed in them. The iron oxide nanoparticles were synthesized by the solvothermal method demonstrating the magnetic properties by acting to the external magnetic field. To increase the local heat superparamagnetic nanoparticles (iron oxide magnetic nanoparticle (IONPs)) of the average size of 20 nm in size and the concentrations from 1 to 10 mg/mL of MNPs with a step size of 1 mg/mL were tested in 10 replicates for each concentration and solvent. Moreover, the temperature changes for dry liver, and 0 mg/mL concentration was checked for calibration and reference purposes. As a sensing system, advanced 16-FBG optical fiber sensors connected to an interrogator were employed allowing the temperature change to be monitored accurately in real time. A maximum temperature of about 142 °C was recorded by a 5 mg/mL concentration of iron oxide nanoparticles dispersed in the agarose solvent.

Keywords: radiofrequency ablation; iron oxide magnetic nanoparticles; fiber Bragg grating (FBG); optical fiber; the sensing system

1. Introduction

Currently, increasing rates of cancer cases and morbidity require advanced treatment approaches. There are several widely employed conventional techniques for cancer care such as surgery, chemotherapy, immunotherapy, gene therapy, and thermal therapy [1,2]. However, traditional treatment methods have some limitations and cannot always fulfill the need for cancer patients facing the drawbacks and side effects. Minimal invasive techniques have attracted interest in cancer treatment as a possible alternative to the surgery offering lower pain, a smaller area of trauma, and the possibility of reaching inaccessible locations inside the tumor [3]. Thermal ablation therapy is considered as a minimally invasive method working on the principle of introducing heat to cancerous cells and eliminating them by generating cytotoxic temperatures over a short period. Depending on the source of ablation, thermal ablation therapies are differentiated as radiofrequency thermal ablation (RFTA), microwave thermal ablation (MWTA), laser ablation (LA), and high-intensity focused ultrasound ablation (HIFU). Among known thermal therapies, radiofrequency ablation has been the focus of interest of many researchers and clinicians offering several advantages: the ability to be deployed for the treatment of many types of tumor can achieve efficient cell elimination, the safe limited demand of resources, and causes less discomfort to patients, with a short recovery period [4,5]. For the radiofrequency ablation procedure, the tissue is placed on the passive electrode presented in a form of a ground pad. Then, an radiofrequency power is passed to the tissue from an RF generator through an active electrode placed in the tumor area, leading to ionic agitation and resulting in focused heat increment around the electrode due to the difference between the small surface area of the active electrode and large area of the passive electrode [6]. There are commercially available RF probes used by clinicians, among which the advanced LeVeen probes offer the reduction in ablation time and pressure during radiofrequency ablation (RFTA) [7].

Despite the advantages proposed by RF ablation in the treatment of cancer and improvements obtained by researchers since the first pioneering work in the 1990s [4], there are still some challenges faced by clinicians. The main limitation during the RFTA ablation is the inadequate bioheat distribution throughout the tissue [6]; most clinicians observed the maximum temperature at the center of the tumor while the temperature at the periphery region is much less [8]. The complication with the effective thermal ablation is caused by the vaporization of the tissue above 100 °C leading to the increase in the tissue impedance preventing the dissipation of the heat on the tissue. Another vital challenge over the RFTA procedure is in accurate temperature monitoring. The ability to control the temperature allows setting the optimal ablation parameters during RFTA and subsequently preventing the undesired heating of the tissue or the reoccurrence of cancer by providing the information concerning when to terminate the process when the desired conditions are reached. [3]. In addition, the capability to adjust the thermal ablation conditions makes it possible for clinicians to plan an adequate protocol to improve the treatment outcome of cancer. The important parameters affecting the tissue damage are the time and temperature of ablation. The temperature of 42 °C is known as a starting point when protein denaturation happens, leading to thermal damage of the tissue [9]. Therefore, the temperature values between 42 and 60 °C are known as a cytotoxicity range. Researchers have determined that the temperature between 60 and 100 °C is the optimal ablative temperature range in order to induce the protein coagulation and reach instantaneous cell death, while the temperature over 100 °C leads to tissue vaporization and carbonization negatively affecting and decaying the size of ablation area [5].

Thermocouples, magnetic resonance imaging (MRI), and computed tomography imaging (CT) are current accurate temperature measurement techniques exploited during thermal therapies of the tumor by clinicians. However, all the existing techniques have their drawback during temperature measurements such as slow response, poor resolution, high cost, and invasiveness [10]. Fiber optic sensors (FOSs) can be proposed as an alternative to the current measurement techniques offering higher resolution and real-time measurement opportunities. In addition, optical fibers are small, non-toxic, minimally invasive, biocompatible (according to ISO 10993 standard), electromagnetically and chemically inert due to the non-metallic composition, highly flexible, and sensitive [3]. The FOS divided into two sensing methods: fiber Bragg grating (FBG) arrays working on the principle of the wavelength division multiplexing and distributed sensing based on frequency domain reflectometry. In FBG, several sensors are inscribed inside the single fiber providing the sensing mechanism in multiple points. However, the main drawback of the FBG consisted of the distance between multiplexed FBGs array sensors. This work proposes the application of the advanced 16-element array FBGs to overcome the existing limitation and demonstrate the best sensing performance during temperature monitoring over a 7.61 cm sensor length.

Moreover, this work investigated the possibility to employ nanoparticles as an approach to achieve homogeneous heat distribution during the thermal ablation process that may prevent the death of healthy cells surrounding the tumor. The widely used type of metallic nanomaterial in RFTA is an iron oxide magnetic nanoparticle (IONP) with a magnetite Fe_3O_4 core [8,11]. Nanoparticles are small nanomaterials of size between 1 nm to 100 nm distinguished by their advanced magnetic, optical, and mechanical properties. In addition, magnetic iron oxide nanoparticles are differentiated by their biocompatibility and high surface-to-area ratio leading to the specific and selective attachment to the cancer area by the surface functionalization opportunities. Magnetic nanoparticles are known for the superior control of energy deposition in the cancer area by only heating the targeted area [12]. The thermal ablation of the tumor loaded with iron oxide magnetic nanoparticles and further exposure to the external electromagnetic field lead to the energy conversion into heat. The heat generation occurs due to the friction occurring between nanoparticles and surrounding the medium based on Neel and Brownian relaxation phenomena and the hysteresis loss [12,13]. The magnetic moment of magnetic nanoparticles subjected to the alternating magnetic field (AMF) tends to line up with the field leading to the dissipation of magnetic energy into thermal energy when the nanoparticles' moment backtracked to the equilibrium [14]. The size of nanoparticles is vital for heat generation and biodistribution within the tissue affecting the possible outcome of thermal therapy. Superparamagnetic nanoparticles with sizes between 10 and 30 nm were found as the best candidate for the temperature increase during ablation. Moreover, the most important parameters of nanoparticles affecting the thermal therapy features are the dispersion concentration and the solvent. The concentration of iron oxide magnetic nanoparticles has a direct relation to the finite sum of generated heat during the treatment. Meanwhile, the dynamic viscosity of the solvent affects the total amount of generated heat by Brownian motion phenomena [12,15]. Hence, the ability to adjust the most relevant parameters of nanoparticles can provide advanced treatment outcomes for clinicians. One of the widely used solvents in biomedical applications is agarose due to its antibacterial property, stability, biocompatibility, and ease of nanoparticle absorption [16,17]. Another biocompatible solvent offering antifungal and antimicrobial properties is chitosan that is also used in anti-cancer treatments and pharmacy [18,19].

The importance of this work consists of the broad investigation of physical parameters such as the concentration and the effect of agarose and chitosan solvents on the thermal ablation properties mediated with 20 nm-sized iron oxide nanoparticles. In order to validate the best heating scenario and determine the optimal heating parameters, 10 replicates of 10 concentrations of nanoparticles starting from 1 to 10 mg/mL dispersed in two different solvents were investigated in this research work. In addition, the implementation of a 16-element array FBG sensing system to measure the spatial temperature profile over the radiofrequency ablation was used for the first time, offering a larger sensing area in real time. This work demonstrated the dependence of the heating effect from the concentration of nanoparticles and the influence of dispersion solvents. The application of nanoparticles during the thermal ablation process provides the opportunity to increase the area of ablation that reaches the instantaneous mortality rate and can be exploited to treat larger tumors. The accurate temperature monitoring in real time recorded the effective heat distribution within the porcine liver tissue when nanoparticles were dispersed in agarose solvent.

2. Materials and Methods

2.1. Experimental Setup

The radiofrequency ablation setup consisting of an RF (radiofrequency) generator, Micron Optics, 16-element array FBG optical fiber, and commercially purchased porcine liver is schematically depicted in Figure 1 with the photographic view of the experimental setup in Figure 2. The customized hybrid radiofrequency ablation (RFA)/Microwave ablation (MWA) generator for research purposes (LEANFA S.r.l., Ruvo di Puglia, Italy, Hybrid RFA/MWA module) coupled with the RF or MW applicator depending on the application was used as a thermal ablation source. This study employed the RF module with a radiofrequency applicator ending with the conical in shape and 0.5 cm in length with an active electrode (AE) at the tip. The dimensions of the applicator are 0.3 cm in diameter and 16 cm in length. The passive electrode (PE) is a metallic plate positioned underneath the tissue.

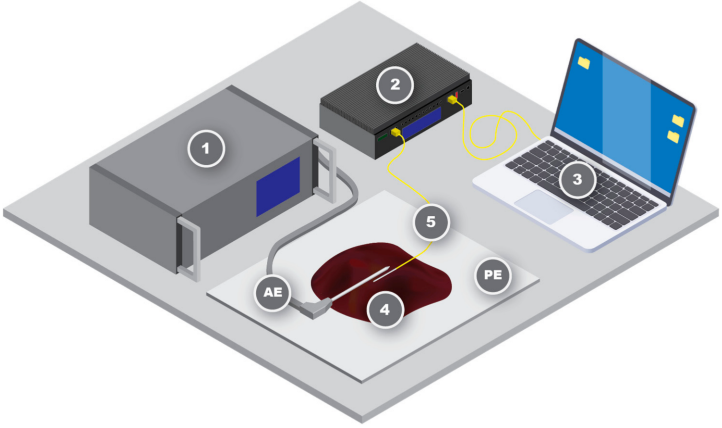

Figure 1. Schematic representation of the radiofrequency ablation setup of the porcine liver using a 16-element array fiber Bragg grating (FBG) temperature sensing system. The setup consisted of: (1) an RFA generator; (2) Micron Optics; (3) computer; (4) porcine liver; (5) 16-element FBG array.

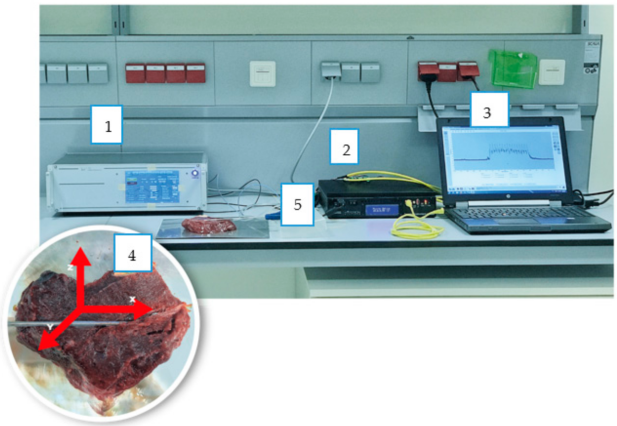

Figure 2. The photographic view of the experimental setup of the radiofrequency ablation mediated with iron oxide nanoparticles. The 16-element array FBG is placed in x-direction on the surface of the porcine liver phantom. The numberings of the equipment, porcine liver and optical fiber are located and marked as in Figure 1.

The porcine liver used for ablation purposes was commercially purchased from the butchery shop and utilized according to the European protocol of “Three Rs” [10]. The phantom was adjusted to room temperature at 22–25 °C for several hours before use to obtain the conditions close to the body temperature. The initial temperature was measured employing the contact thermocouple IKA ETS–D5.

The porcine liver was exposed to the radiofrequency ablation (RFTA) using an applicator connected to an RF generator with the operating frequency of 450 kHz and at the power of 50 W maintained in the same conditions for all sets of trials. The RF generator was maintained at a ‘safe mode on’ state that allowed to automatically terminate the power while reaching the set tissue impedance of 800 Ω controlled by the impedance meter, included within the RF applicator.

The 20 nm iron oxide nanoparticles at different concentrations were introduced ex vivo on the tissue surface. Thermal ablation experimental trials were repeated at 10 replicates for each set of concentrations starting from 1 mg/mL to 10 mg/mL for both agarose and chitosan solvents. Two types of solvents, such as 0.2% agarose solvent and 0.5 wt. % chitosan solvent, were exploited to derive experimentally the best performing solvent and investigate the heating mechanism. The stock solvents for each concentration were prepared and finally, 100 µL of the nanoparticle solvents were injected on the porcine liver surface using a syringe. The experiments lasted for 120 s for all trials.

The temperature sensing system consists of 16-element array FBGs attached alongside with applicator and its tip in close proximity in x-direction as shown in Figure 2 to observe the temperature change. The whole distance between the first and the last FBGs was 7.61 cm, which can be considered as the sensing area of the experiment. The measuring fiber was analyzed using an optical sensing interrogator (si255, Micron Optics) at the continuous measurement conditions (1 kHz speed). The interrogator was set to monitor 16 peaks on the measured spectrum, using fast-tracking polynomial fitting over a spectral threshold [20].

The time step between each measurement was equal to 1 millisecond. After converting the spectral shifts of each peak to thermal data, it was possible to reconstruct the temperatures of the FBGs along the length of the fiber during the heating procedure. Using these thermal values and the previously mentioned distances, the interpolation was implemented to estimate the temperatures at points between the FBGs. The resulting spatial resolution between data points was equal to 0.0001 m.

2.2. FBG Array Fiber Fabrication, Calibration, and Characterization

The fiber Bragg grating (FBG) array used for the thermometry was inscribed with the point-by-point technique using femtosecond laser radiation [21]. The method enables FBGs inscription through a polyimide protective coating of a fiber resulting in durability and high mechanical strength of a fabricated sensor [22]. The high degree of flexibility makes the method most suitable for writing FBGs with different resonant wavelengths and different lengths [21], with specified refractive index profile [23], and an arbitrary position in the cross-section of fiber [24]. A Fibercore SM1500 (9/125) P fiber with a 20 µm-thick polyimide protective coating was used for the fabrication of an FBG array enclosing 16 FBGs. Each FBG in the array has a length of 1 mm and a distance between adjacent FBGs of 5.000 mm, so the total (edge-to-edge) length of the FBG array was 76 mm. In order to separate FBGs in spectral-domain resonant wavelengths were distributed equidistantly in the range of 1520–1580 nm with $\Delta\lambda \approx 4$ nm (Figure 3).

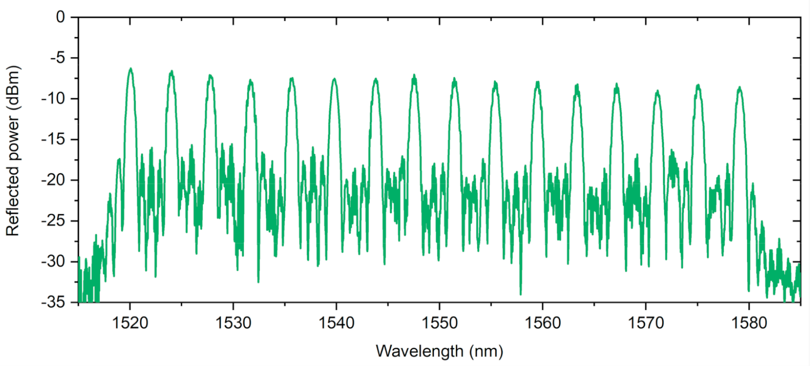

Figure 3. The reflection spectrum of a sensor array containing 16 FBGs.

The calibration of 16-element array FBG fibers was conducted before the experiments. The spectra for each temperature from 23 to 55 °C with 2 °C increments were recorded. The shifts of wavelengths corresponding to each FBG were observed for each temperature change, which is demonstrated in Figure 4. The resulting value of constant temperature coefficient k was approximately 8.8 pm/K.

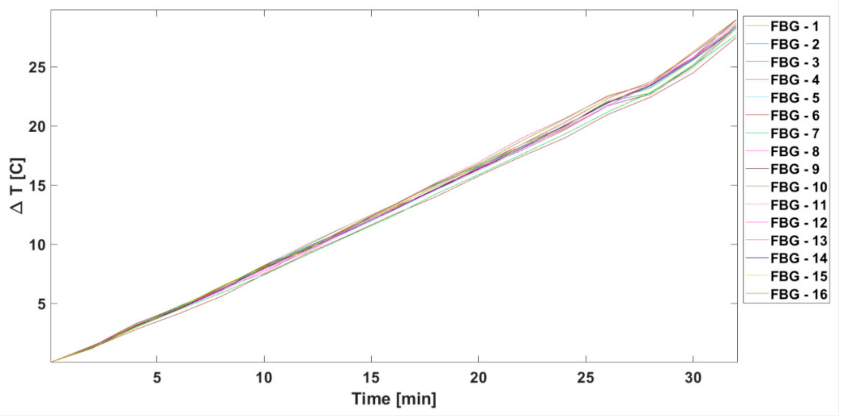

Figure 4. Sixteen-element array FBG fiber calibration.

2.3. Iron Oxide Magnetic Nanoparticles Synthesis and Characterization

The iron oxide magnetic nanoparticles were synthesized employing the solvothermal method according to the Reference [25]. The Fe(II) and Fe(III) iron sources were weighed and placed into 50 mL beaker. The beaker containing 2.535 g of $FeCl_3 \times H_2O$ and 1.8625 g of $FeCl_2 \times 4H_2O$ followed by the addition of 6.25 mL distilled water under the magnetic stirring on a hotplate. 6.25 mL of 25% ammonium hydroxide was added slowly in the fume hood to the iron salt solution with continuous stirring at 700 rpm for 2 min. The obtained final 15 mL solution was poured into the 30 mL Teflon-lined stainless steel autoclave that was further put into the muffle furnace for 1 h heating at 180 °C. The obtained nanoparticles were washed three times using the distilled water and separated using an external SuperMag magnet. Purified iron oxide nanoparticles were dried in an oven at 40 °C to obtain the powder. Finally, the nanoparticles were characterized by using an X-Ray diffraction instrument (Figure 5) and scanning electron microscopy (Figure 6).

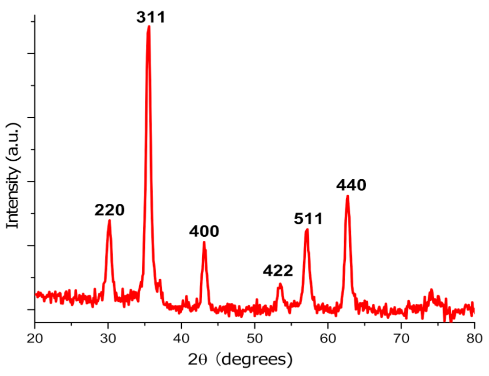

Figure 5. XRD analysis peaks for 20 nm iron oxide nanoparticles.

Figure 5 presents the data obtained from the Rigaku SmartLab X-ray diffraction (XRD) system demonstrating the diffraction peaks at 30.14°, 35.48°, 43.08°, 53.47°, 57.02°, 62.6° standing for diffraction values of [220], [311], [400], [422], [511] and [440] planes of Fe_3O_4 crystals, respectively, which matched the literature data for magnetites [26]. The XRD data allowed us to validate the crystal structure of synthesized iron oxide nanoparticles and estimate the approximate size of approximately 20 nm using Scherrer's equation.

The morphological analysis of iron oxide nanoparticles was obtained using a Scanning Electron Microscope (SEM, Auriga Crossbeam 540) that is presented in Figure 6. The SEM micrograph demonstrates the uniformly distributed nanoparticles of spherical shapes.

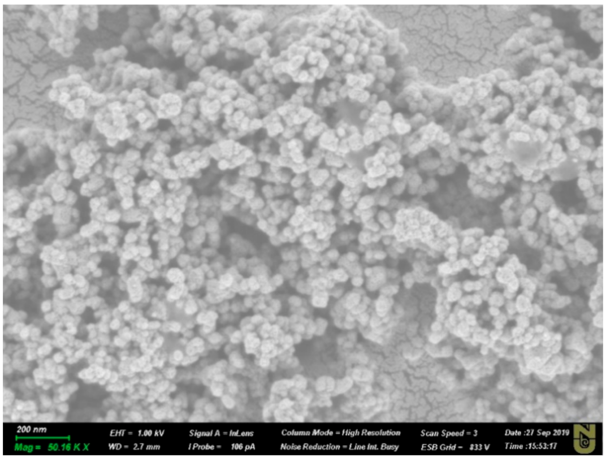

Figure 6. The SEM micrograph of 20 nm oxide nanoparticles obtained using Scanning Electron Microscopy at 50.16 KX magnitude validating the spherical shape of the synthesized nanoparticles.

3. Results

This study mainly analyzed the influence of concentration and dispersion solvents on the heating effect and heat distribution during the radiofrequency ablation of the porcine liver when the tissue was injected ex vivo with the 20 nm iron oxide nanoparticles. All of the shifts over the length of each experiment were converted to temperature changes using the calibration data. The example of the obtained graphs for one of the experiments (5 mg/mL agarose solvent) can be seen in Figure 7.

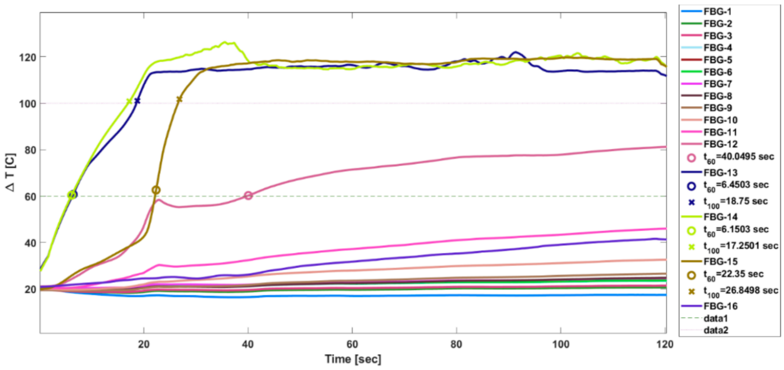

Figure 7. Temperature changes were obtained by the 16-element array FBGs recorded on the continuous mode using the Micron Optics instrument. (The 12–16 FBGs presented the temperature sensing record over time due to the proximity to the RF electrode tip).

Figure 7 demonstrated the temperature increase over time. As can been seen from the graph, the desired temperature increase between 60 and 100 °C recorded by the FBG #12–15 located in the vicinity to the tip of the RF applicator occurred after approximately 5 s until 25 s. The obtained data could provide relevant information when the ablation process should be terminated to achieve the effective thermal ablation process. Moreover, the thermal map of the ablation outcomes on the tissue is demonstrated in Figure 8 during the application of iron oxide nanoparticles dispersed in agarose solvent for the radiofrequency ablation process. The thermal map presents the heating range between 42, 60, and 100 °C over time with the change in the ablation area.

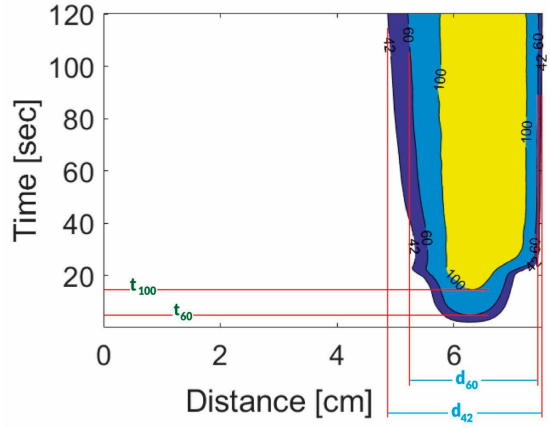

Figure 8. The thermal map obtained during the thermal ablation of the porcine liver when 5 mg/mL iron oxide nanoparticles dispersed in agarose were employed, where t_{60}—time needed to reach the temperature 60 °C; t_{100}—time needed to reach the temperature 100 °C; d_{42}—the ablated area when the temperature reached 42 °C; and d_{60}—the ablated area when the temperature reached 60 °C.

Liver tissue in the ablation area is about 3–4 cm, and each sample is different. Considering that, from References [6,10], it appears that the ablation is more extended towards the planar direction than through the depth having a teardrop shape, the tissue in the outer range of the organ never becomes hot. This was also visually checked and with a thermal camera during the experimentsGiven that the tissue encloses the whole ablation area, the experiments hereby designed do not provide an expected ablation area that exceeds the volume of the tissue; for this reason, the tissue thickness was not playing a significant effect, in comparison with the other thermo-electrical properties.

The changes of temperature increment during RFTA for 10 concentrations of iron oxide nanoparticles dispersed in both solvents were recorded and consolidated in Table 1. According to the recorded experimental data, the area near the point corresponding to FBGs#12–16 was the most sensitive due to its close placement to the active electrode. Similar observations were made for the majority of the experiments. Hence, it was decided to use the values obtained from these sensors of 16-element array FBGs for further data analysis. For each concentration of nanoparticles dispersed in both solvents of agarose and chitosan, the average values of the maximum temperature and time to reach the temperatures of 60 and 100 °C for all 10 replicates are shown.

Table 1. The relation between the concentration of iron oxide magnetic nanoparticles (IONPs), time, and temperature obtained during radiofrequency thermal ablation (RFTA).

Concentration of IONP (mg/mL)	Time to Reach 60 °C (s)		Time to Reach 100 °C (s)		Maximum Temperature (°C)	
	AGAROSE Solvent	CHITOSAN Solvent	AGAROSE Solvent	CHITOSAN Solvent	AGAROSE Solvent	CHITOSAN Solvent
0	5.58	6.48	14.94	16.53	133.03	136.11
1	6.09	7.11	17.15	18.21	130.60	143.27
2	4.53	7.77	13.14	19.44	139.36	137.67
3	7.08	6.48	16.53	19.17	124.98	130.94
4	7.44	7.38	22.14	18.90	122.33	129.80
5	5.37	6.96	15.75	18.96	141.88	135.27
6	5.52	6.75	15.18	19.08	138.60	137.99
7	5.61	6.66	14.73	21.78	136.50	133.02
8	5.76	7.50	16.38	19.80	130.16	149.56
9	5.61	7.11	16.05	18.24	126.62	135.89
10	5.19	7.26	13.56	19.86	134.99	137.19

According to the summarized data of the temperature increase over time, the maximum temperature increment recorded was 149 °C for iron oxide nanoparticles dispersed in chitosan solvent with a concentration of 8 mg/mL. However, the experimental results demonstrated that nanoparticles dispersed in agarose solvent presented a better performance and heating effect compared to the chitosan solvent at the same concentrations. For instance, as shown in Table 2, the time to reach 60 °C is quicker for IONPs at the concentration of 5 mg/mL in agarose solvent compared to the same concentration of IONPs in the chitosan solvent. In addition, the maximum temperature reached by IONPs at the concentration of 5 mg/mL in chitosan solvent was 135.27 °C during RFTA while the IONPs dispersed in agarose solvent performed better and showed the maximum temperature of about 142 °C.

The area of tumor ablation is considered one of the main challenges during thermal ablation therapy. Figure 9 presents the values of the ablated diameters achieved at 42 °C (t_{42}) for all 10 concentrations and both solvents. The ablation diameter achieved by iron oxide nanoparticles for chitosan and agarose solvents reached approximately 3 cm as can be seen from Figure 9.

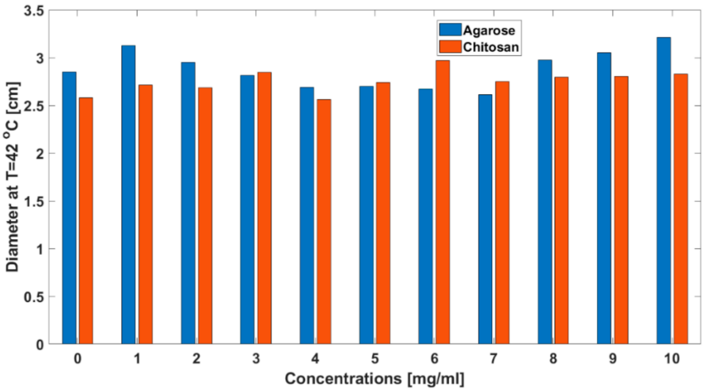

Figure 9. The maximum ablation area was reached during RFTA at different concentrations of iron oxide nanoparticles when the ablation temperature reached 42 °C.

Figure 10 demonstrates the comparative chart of the ablated diameter achieved during radiofrequency ablation when the temperature increment reached 60 °C (t_{60}). The chart includes broad information regarding the influence of concentration in 10 replicates for both solvents at $t_{60.}$ The maximum diameter achieved during the ablation process was approximately 2.5 cm.

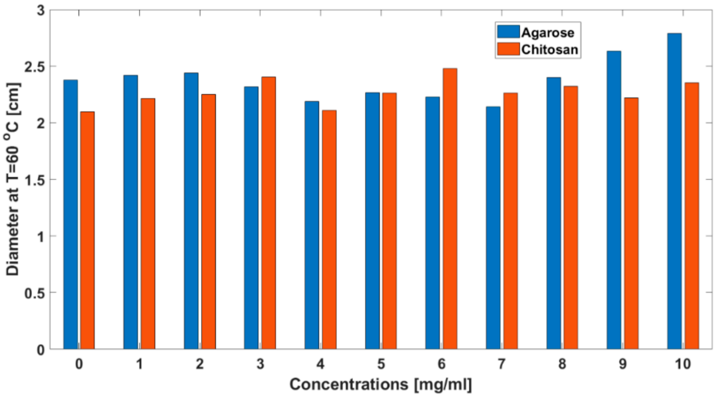

Figure 10. The maximum ablation area was reached during RFTA at different concentrations of iron oxide nanoparticles when the ablation temperature reached 60 °C.

Table 2. The mean and standard deviation values were obtained during the RFTA for all 10 concentrations of nanoparticles dispersed in both solvents.

IONP Concentration mg/mL	TMAX, °C				t_{60}, s				d_{60}, cm				d_{42}, cm			
	Agarose		Chitosan		Agarose		Chitosan		Agarose		Chitosan		Agarose		Chitosan	
	Mean Value	Standard Deviation	Mean Value	Standard Deviation	Mean Value	Standard Deviation	Mean Value	Standard Deviation	Mean Value	Standard Deviation	Mean Value	Standard Deviation	Mean Value	Standard Deviation	Mean Value	Standard Deviation
0	133.03	17.09	136.11	22.94	5.58	1.96	6.48	1.14	2.38	0.42	2.09	0.34	2.85	0.43	2.58	0.46
1	130.60	14.82	143.27	17.89	6.09	1.37	7.11	1.83	2.42	0.35	2.22	0.53	3.12	0.62	2.72	0.65
2	139.36	21.46	137.67	24.64	4.53	1.20	7.77	1.40	2.44	0.53	2.25	0.34	2.95	0.57	2.68	0.34
3	124.98	8.63	130.94	19.55	7.08	3.32	6.48	1.08	2.32	0.39	2.40	0.44	2.81	0.39	2.85	0.50
4	122.33	11.93	129.80	15.17	7.44	2.96	7.38	1.71	2.19	0.46	2.11	0.24	2.69	0.44	2.56	0.30
5	141.88	22.84	135.27	17.81	5.37	1.76	6.96	1.78	2.27	0.36	2.26	0.38	2.70	0.31	2.74	0.41
6	138.60	16.84	137.99	20.76	5.52	1.32	6.75	1.45	2.23	0.31	2.48	0.74	2.67	0.31	2.97	0.79
7	136.50	20.72	133.02	17.75	5.61	1.74	6.66	1.28	2.14	0.19	2.26	0.43	2.61	0.20	2.75	0.44
8	130.16	20.43	149.56	18.99	5.76	0.93	7.50	1.39	2.40	0.43	2.32	0.26	2.98	0.52	2.79	0.30
9	126.62	13.87	135.89	17.46	5.61	2.24	7.11	2.15	2.63	1.43	2.22	0.47	3.05	1.36	2.80	0.57
10	134.99	20.56	137.19	19.94	5.19	1.88	7.26	1.39	2.79	1.58	2.35	0.79	3.21	1.55	2.83	0.80

According to the temperature sensing measurements, the agarose and chitosan solvents provided different heating patterns affecting to maximum temperature (T_{MAX}) achieved during radiofrequency ablation. The Figure 11A,B presented the processed values of temperatures achieved during RFTA with the averaged values for all 10 trials for each concentration. In addition, the graph demonstrated the error bars that are fluctuating widely.

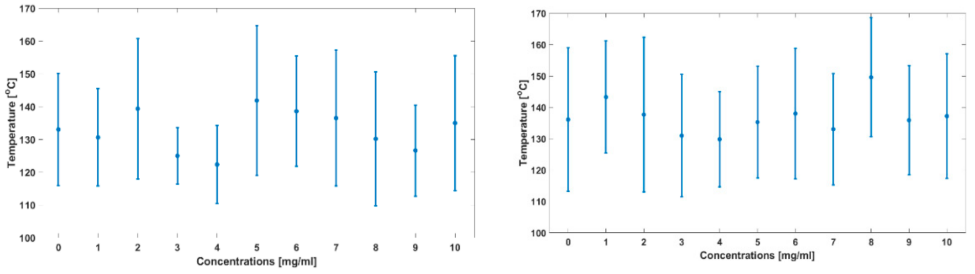

(**A**) (**B**)

Figure 11. The maximum temperature reached during the radiofrequency ablation of porcine liver loaded with 20 nm iron oxide nanoparticles dispersed: (**A**) in agarose solvent; and (**B**) in chitosan solvent.

4. Discussion

The heating mechanism during RFTA using superparamagnetic iron oxide magnetic nanoparticles of 20 nm in size is explained mainly by the Neel and Brownian relaxation depicted in Figure 12. During the Neel relaxation, the magnetic nanoparticles applied to the external electromagnetic moment rotate within the crystal to align with the magnetic moment, while during the Brownian motion, the rotation of particles happens to align the magnetic moment that is enclosed to the crystal axis as depicted in Figure 12 [27]. Hence, the superparamagnetic nanoparticles of 20 nm in size produce the increment of heat absorbing the electromagnetic energy when the particle moment tends to return to its equilibrium state [28]. The size of nanoparticles used for the thermal ablation procedure is vital and varied between 10 and 30 nm in order to have single domain superparamagnetic nanoparticles. The other vital parameters of nanoparticles used for the thermal therapy are the concentration of nanoparticles that is in direct proportion to the sum of the generated heat, and the dynamic viscosity that influences the amount of generated heat by Brownian relaxation. The solvents with higher viscosity affect the Brownian rotation phenomena leading to the decrease in heat generation [15]. Moreover, it is preferable to inject the lower concentration of nanoparticles to prevent the negative impact of high concentrations and ease of washing out from the body.

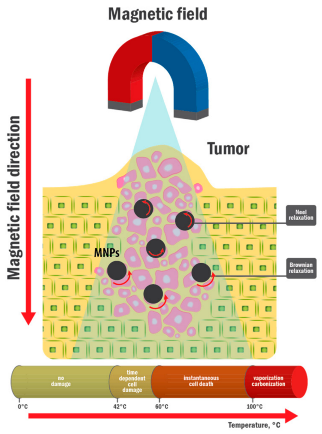

Figure 12. The schematic representation of the physical mechanism of electromagnetic energy transfer into heat when nanoparticles are used.

The studies regarding the thermal dosimetry for optimal thermal ablation therapy demonstrated the demand in the achievement of cytotoxicity heat range between 42 °C and 60 °C in order to get the protein coagulation and cell damage as can been seen from the scale in Figure 12. However, it is important to prevent the heat of the cells at a temperature higher than 100 °C because at this range, the vaporization and carbonization of tissue happen which decreases the heating outcome [9]. Therefore, the broad investigation of the impact of nanoparticles during the thermal ablation procedure provides the advanced protocol to optimize the time and concentration of nanoparticles to terminate the process when the desired parameters were obtained. Table 2 provides the extensive results of the maximum temperatures obtained during RFTA along with the maximum ablated diameters (d_{60} and d_{42}) reached at temperatures of 42 and 60 °C including the mean value and standard deviations recorded during 10 trials of experimental studies.

The current research involved 200 experimental trials conducted for 10 concentrations of IONPs dispersed in two solvents among 10 trials in order to evaluate the heating properties of nanomaterials that were measured using the 16-element array FBGs. It is important to note that for all the trials, the single 16-element array FBG sensing system was employed, demonstrating the accurate temperature recording without diminishing its property over the measurements. In addition, the sensing system validated that the temperature increment over 42 °C occurs only at an area of close proximity to the electrode tip and where the nanoparticles were introduced, which made it possible to prevent the overheating of the surrounding area.

The estimated results brought to the conclusion that the magnetic nanoparticles dispersed in both solvents behave similarly regarding the increase in the ablation area and reaching the maximum temperature, however, agarose demonstrated better heating features by reaching the cytotoxicity temperature ranges in a shorter time and lower concentrations compared to the IONPS dispersed in chitosan solutions.

5. Conclusions

The proposed work was performed in order to determine the advanced outcomes that nanoparticles can bring to thermal ablation therapy. The main issue during radiofrequency ablation consisted of the possibility of damage to cells surrounding the tissue. Moreover, the accurate temperature measurement system in real time is another limitation occurring during thermal ablation procedures. The synthesized iron oxide nanoparticles demonstrated good heating effects, making it possible to achieve the highest temperature in a short period. The investigations of 10 different concentrations allowed defining the concentration of 5 mg/mL as having the best outcome. In addition, the analysis of two possible solvents such as agarose and chitosan to disperse and inject the nanoparticles ex vivo onto the phantom liver conceded to conclude that agarose demonstrates the better performance in terms of reaching the temperature of 142 °C at 5 mg/mL concentration in a shorter time compared to the chitosan solvent.

The application of a 16-element array FBG sensor for temperature monitoring during RFTA could eliminate the drawback of ordinary FBG sensors hindered by the distance between sensors allowing them to obtain accurate temperature monitoring in real time. The used sensing technique presented the precise temperature measurement performance during all 200 trials. The proposed setup with the heating outcome could be extended further for the clinical applications.

Author Contributions: Conceptualization, Z.A. and D.T.; methodology, Z.A., A.A. (Arman Aitkulov), D.T., A.W. and A.D.; software, A.A. (Arman Aitkulov); validation, Z.A., A.A. (Arman Aitkulov), D.T. and V.J.I.; formal analysis, A.A. (Arman Aitkulov); investigation, all authors; resources, D.T.; data curation, A.A. (Arman Aitkulov) and Z.A.; writing—original draft preparation, Z.A.; writing—review and editing, all authors; visualization, Z.A.; supervision, D.T. and V.J.I.; funding acquisition, D.T. All authors have read and agreed to the published version of the manuscript.

Funding: The research was funded mainly by Nazarbayev University, under grants SMARTER (code: 091019CRP2117) and EPICGuide (code: 240919FD3908). A.W. and A.D. acknowledge the support of the Ministry of Education and Science of the Russian Federation (14.Y26.31.0017).

Institutional Review Board Statement: Not applicable.

Informed Consent Statement: Not applicable.

Acknowledgments: The research was funded mainly by Nazarbayev University, under grants SMARTER (code: 091019CRP2117) and EPICGuide (code: 240919FD3908). A.W. and A.D. acknowledge the support of the Ministry of Education and Science of the Russian Federation (14.Y26.31.0017). Authors acknowledge D. Balmassov for the support in drawing Figures 1 and 12.

Conflicts of Interest: The authors declare no conflict of interest.

References

1. IARC. *Latest Global Cancer Data*; International Agency for Research on Cancer: Lyon, France, 2018.
2. Dutz, S.; Hergt, R. Magnetic particle hyperthermia—A promising tumour therapy? *Nanotechnology* **2014**, *25*, 452001. [CrossRef]
3. Schena, E.; Tosi, D.; Saccomandi, P.; Lewis, E.; Kim, T. Fiber Optic Sensors for Temperature Monitoring during Thermal Treatments: An Overview. *Sensors* **2016**, *16*, 1144. [CrossRef] [PubMed]
4. Macchi, E.G.; Tosi, D.; Braschi, G.; Gallati, M.; Cigada, A.; Busca, G.; Lewis, E. Optical fiber sensors-based temperature distribution measurement inex vivoradiofrequency ablation with submillimeter resolution. *J. Biomed. Opt.* **2014**, *19*, 117004. [CrossRef]
5. Goldberg, S. Radiofrequency tumor ablation: Principles and techniques. *Eur. J. Ultrasound* **2001**, *13*, 129–147. [CrossRef]
6. Lencioni, R.; Crocetti, L.; Cioni, D.; Della Pina, C.; Bartolozzi, C. Percutaneous Radiofrequency Ablation of Hepatic Colorectal Metastases Technique, Indications, Results, and New Promises. *Investig. Radiol.* **2004**, *39*, 689–697. [CrossRef] [PubMed]
7. Nakamuta, M.; Kohjima, M.; Morizono, S.; Yoshimoto, T.; Miyagi, Y.; Sakai, H.; Enjoji, M.; Kotoh, K. Comparison of tissue pressure and ablation time between the LeVeen and cool-tip needle methods. *Comp. Hepatol.* **2006**, *5*, 10. [CrossRef] [PubMed]
8. Ashikbayeva, Z.; Tosi, D.; Balmassov, D.; Schena, E.; Saccomandi, P.; Inglezakis, V. Application of Nanoparticles and Nanomaterials in Thermal Ablation Therapy of Cancer. *Nanomaterials* **2019**, *9*, 1195. [CrossRef] [PubMed]
9. Sapareto, S.A.; Dewey, W.C. Thermal dose determination in cancer therapy. *Int. J. Radiat. Oncol. Biol. Phys.* **1984**, *10*, 787–800. [CrossRef]
10. Palumbo, G.; Iadicicco, A.; Tosi, D.; Verze, P.; Carlomagno, N.; Tammaro, V.; Ippolito, J.; Campopiano, S. Temperature profile of ex-vivo organs during radio frequency thermal ablation by fiber Bragg gratings. *J. Biomed. Opt.* **2016**, *21*, 117003. [CrossRef]
11. Beik, J.; Abed, Z.; Ghoreishi, F.S.; Hosseini-Nami, S.; Mehrzadi, S.; Shakeri-Zadeh, A.; Kamrava, S.K. Nanotechnology in hyperthermia cancer therapy: From fundamental principles to advanced applications. *J. Control. Release* **2016**, *235*, 205–221. [CrossRef]
12. Suriyanto, N.; Ng, E.Y.K.; Kumar, S.D. Physical mechanism and modeling of heat generation and transfer in magnetic fluid hyperthermia through Néelian and Brownian relaxation: A review. *Biomed. Eng. Online* **2017**, *16*, 1–22. [CrossRef] [PubMed]
13. García-Jimeno, S.; Ortega-Palacios, R.; Cepeda-Rubio, M.; Vera, A.; Leija, L.; Estelrich, J. Improved thermal ablation efficacy using magnetic nanoparticles: A study in tumor phantoms. *Prog. Electromagn. Res.* **2012**, *128*, 229–248. [CrossRef]
14. Hergt, R.; Andra, W.; D'Ambly, C.; Hilger, I.; Kaiser, W.; Richter, U.; Schmidt, H.-G. Physical limits of hyperthermia using magnetite fine particles. *IEEE Trans. Magn.* **1998**, *34*, 3745–3754. [CrossRef]
15. Dennis, C.L.; Ivkov, R. Physics of heat generation using magnetic nanoparticles for hyperthermia. *Int. J. Hyperth.* **2013**, *29*, 715–729. [CrossRef]
16. Amiri, S.; Mehrnia, M.R.; Sobhanifard, S.; Roudsari, F.P.; Hoseini, S.-N. Evaluation of agarose-entrapped magnetic nanoparticles influence on protein adsorption isotherm and kinetics using nickel-iminodiacetic acid ligand. *Sep. Purif. Technol.* **2017**, *188*, 423–430. [CrossRef]
17. Ma, X.; Xia, Y.; Ni, L.; Song, L.; Wang, Z. Preparation of gold nanoparticles–agarose gel composite and its application in SERS detection. *Spectrochim. Acta Part. A Mol. Biomol. Spectrosc.* **2014**, *121*, 657–661. [CrossRef]
18. Singh, M.K.; Prajapati, S.K.; Mahor, A.; Rajput, N.; Singh, R. Chitosan: A Novel Excipient in Pharmaceutical Formulation: A Review. *Int. J. Pharm. Sci. Res.* **2011**, *2*, 2266–2277.
19. Singla, A.K.; Chawla, M. Chitosan: Some pharmaceutical and biological aspects—An update. *J. Pharm. Pharmacol.* **2001**, *53*, 1047–1067. [CrossRef] [PubMed]
20. Tosi, D. Review and Analysis of Peak Tracking Techniques for Fiber Bragg Grating Sensors. *Sensors* **2017**, *17*, 2368. [CrossRef]
21. Dostovalov, A.; Wolf, A.; Parygin, A.; Zyubin, V.; Babin, S. Femtosecond point-by-point inscription of Bragg gratings by drawing a coated fiber through ferrule. *Opt. Express* **2016**, *24*, 16232–16237. [CrossRef]
22. Bernier, M.; Trépanier, F.; Carrier, J.; Vallée, R. High mechanical strength fiber Bragg gratings made with infrared femtosecond pulses and a phase mask. *Opt. Lett.* **2014**, *39*, 3646–3649. [CrossRef]
23. Williams, R.J.; Voigtländer, C.; Marshall, G.D.; Tünnermann, A.; Nolte, S.; Steel, M.J.; Withford, M.J. Point-by-point inscription of apodized fiber Bragg gratings. *Opt. Lett.* **2011**, *36*, 2988–2990. [CrossRef]

24. Wolf, A.; Dostovalov, A.; Bronnikov, K.; Babin, S. Arrays of fiber Bragg gratings selectively inscribed in different cores of 7-core spun optical fiber by IR femtosecond laser pulses. *Opt. Express* **2019**, *27*, 13978–13990. [CrossRef]
25. Ozel, F.; Kockar, H.; Karaagac, O. Growth of Iron Oxide Nanoparticles by Hydrothermal Process: Effect of Reaction Parameters on the Nanoparticle Size. *J. Supercond. Nov. Magn.* **2015**, *28*, 823–829. [CrossRef]
26. Wang, W.; Zheng, L.; Lu, F.; Hong, R.; Chen, M.Z.Q.; Zhuang, L. Facile synthesis and characterization of magnetochromatic Fe3O4 nanoparticles. *AIP Adv.* **2017**, *7*, 056317. [CrossRef]
27. Rosensweig, R. Heating magnetic fluid with alternating magnetic field. *J. Magn. Magn. Mater.* **2002**, *252*, 370–374. [CrossRef]
28. Day, E.S.; Morton, J.G.; West, J.L. Nanoparticles for Thermal Cancer Therapy. *J. Biomech. Eng.* **2009**, *131*, 074001. [CrossRef]